MTLA 46 (2026) 102709

Contents lists available at ScienceDirect

Materialia

journal homepage: www.elsevier.com/locate/mtla

Full Length Article

Increasing SiGe crystal growth rate utilizing microgravity

Yasutomo Arai [a,*], Kyoichi Kinoshita [b], Toshinori Taishi [c], Yusuke Matsuoka [d], Taichi Abe [d], Takao Tsukada [e], Masaki Kubo [f]

[a] Japan Aerospace Exploration Agency, 2-1-1 Sengen, Ibaraki, Tsukuba 305-8505, Japan
[b] School of Science and Technology, Meiji University, Kawasaki 214-8571, Japan
[c] Faculty of Engineering, Shinshu University, 4-17-1, Wakasato, Nagano, 380-8553, Japan
[d] National Institute for Materials Science, Sengen, Tsukuba 305-0047, Japan
[e] New Industry Creation Hatchery Center, Tohoku University, 6-6-10 Aramaki, Aoba-ku, Sendai, Miyagi, 980-8579, Japan
[f] Department of Chemical Engineering, Graduate School of Engineering, Tohoku University, 6-6-07 Aramaki, Aoba-ku, Sendai, Miyagi, 980-8579, Japan

ARTICLE INFO

Keywords:
Silicon germanium alloy
Crystal growth (3647, 3862)
Solid/liquid interface (2663)
Microsegregation (1358)
Soret effect (1243)

ABSTRACT

An unanticipated rapid increase in the initial growth rate has been reported in solid-solution semiconductor crystal growth experiments aboard the International Space Station (ISS). This study reports the growth rate of a $Si_{52}Ge_{48}$ solid-solution crystal grown on the ISS using the Traveling Liquidus Zone (TLZ) method, with a diameter of 20 mm and a growth length of 18.8 mm at the center axis. The average growth rate was 0.125 mm/h over a 150 h growth period. The growth interface during growth was identified by artificial striations induced by the temperature-step method. In the initial transient region, with a growth length of 1.5 mm, the solid/liquid interface transitioned from a planar to a facet array, and after the facets disappeared, the interface reverted to planar. These planar growth rates were faster than the average growth rate of 0.125 mm/h. Further, the facet growth rate was calculated. Tiller's criteria indicated that constitutional supercooling had occurred in the initial transient growth region. The unanticipated rapid increase in growth rate in our experiment was attributed to constitutional supercooling induced by the convectionless condition rather than to the Soret effect.

1. Introduction

Solid-solution silicon-germanium (SiGe) alloys are promising materials for high-performance transistors [1,2], thermoelectric devices [3–5], and infrared lenses [6] because their physical properties, such as the lattice constant and refractive index, can be controlled by the concentration ratio. Thus, controlling the concentration distribution in a bulk SiGe crystal is a crucial technology for any application.

Since a SiGe alloy is a solid-solution system, it has been difficult to grow bulk crystals with concentration control in the melt using conventional growth methods, such as the Czochralski (Cz), Floating Zone, Bridgeman, and traveling-solution methods under terrestrial conditions [7–11]. The Traveling Liquidus Zone (TLZ) method has the advantage of producing homogeneous concentration solid solutions: the crystal growth rate and the concentration of solute in the melt can be determined simultaneously by controlling the positive temperature gradient in the melt produced by a heater [12,13]. The crystal grows toward the high temperature region and the feed on the melt dissolves continuously. In addition, the whole melt keeps saturated in steady state. Further, no transient concentration change has been observed at the initial stage of growth. The planar growth rate of SiGe alloys using the TLZ method, which avoids constitutional supercooling, is usually lower than 0.3 mm/h (near the $Si_{50}Ge_{50}$ concentration), two or three orders of magnitude slower than that of pure silicon. Therefore, attempts to increase the growth rate while maintaining concentration homogeneity and crystal qualities are valuable for applications.

The relationship between the growth rate and growth-interface instabilities, including facet formation in SiGe crystals, has been studied through in-situ observations [14–16]. In addition, Phase-Field Model (PFM) calculations [17–19] have been performed for high growth rates and with forced Si flows in the melt. Studies on Si facet and faceted groove coarsening are being conducted through in-situ observation experiments [20,21]. Changes in the microstructure due to increased growth rate caused by supercooling are a principal issue. These efforts have been dedicated to elucidating the facet-formation mechanism of Si and SiGe grown by the Cz method, based on crystal-microstructure analysis [22,23].

Microgravity promises to prevent convection in a melt, thereby

* Corresponding author.
E-mail address: arai.yasutomo@jaxa.jp (Y. Arai).

https://doi.org/10.1016/j.mtla.2026.102709
Received 20 August 2025; Accepted 5 March 2026
Available online 8 March 2026

expanding the synthetic concentration range [24] and avoiding contact with a container [25,26] and reducing crystal defects. Since the Apollo era, crystal growth experiments have been conducted continuously in space using diffusion-limited growth [27,28], but growth rate control, which is essential for practical applications, has not been achieved. Experiments have also been conducted under microgravity and terrestrial conditions to clarify the effect of convection in the melt on the microstructure formed by dendritic solidification of metals [29–33].

In experiments on alloy semiconductor crystal growth using the Gradient Heating Furnace (GHF) on the ISS [34], a non-axisymmetric crystal growth interface and the concentration [35,36] have been observed, as has isolated nucleation in the melt at the front of the crystal growth interface due to constitutional supercooling at the initial stage [37]. Further, new phenomena were reported, including an unexpected rapid increase in growth rate due to a high concentration gradient in front of the solidification interface, for undetermined reasons [38]. Although an increase in the diffusion constants relative to ground experiments during growth have been proposed to clarify the growth rate increase [39], the Soret effect has not been analyzed.

In this report, we present the details of the growth rate of the planar S/L interface and facet growth rate by precisely analyzing the microstructures and concentration distribution of a SiGe crystal grown by the TLZ method aboard the ISS. We also evaluate the growth-interface instabilities in the initial transition region using Tiller's criterion.

2. Experimental procedure

A metal cartridge containing raw Si and Ge crystals was launched to the ISS on NG-15 (Feb. 2021) and returned to Earth on Crew-3 (May 2022). The procedure for the SiGe crystal growth experiment using the TLZ method with GHF onboard the ISS, and the sample preparation method (e.g., vacuum-sealing the crystals), were described in a previous report [34].

The raw materials were as follows: the single crystal seed Si (p-2.5 kΩcm) <100> was 20.2 mm long and 20 mm in diameter; the Ge (non-doped) was 20 mm long and 20 mm in diameter, sandwiched by the seed and the feed Si; the feed Si was 20.5 mm long and 20 mm in diameter. The carbon spring pressed the feed Si to maintain contact with the melted Ge. The carbon cell and spring were made of 610HU carbon, manufactured by Toyo Carbon. The outer surface of the metal cartridge was blackened to suppress any emissivity change during crystal growth.

The position and the temperature changes of the GHF central heater are shown in Fig. 1a and b. When the heater returned to the crystal growth position from the preheating position shown in Fig. 1a (at the end of sequence B), the elapsed time was reset to zero. The raw Ge material did not melt during preheating in the heater position (A). The preheated heater was returned to the crystal growth position at 600 mm/h (B in Fig. 1a). The heater remained in place for 50 h, then moved toward the crystal growth direction at 0.10 mm/h for 100 h. The duration of crystal growth was 150 h.

An overshoot of the heater temperature was observed around the end of the sequence B in Fig. 1a and the temperature gradually decreased until step 2 (+1.0 °C) was applied at the elapsed time of 1.5 h, as shown in Fig. 1c. Since the SiGe crystal was contained in the carbon cell, the quartz tube, and the metal cartridge, the temperature changing of the crystal by the steps should not be steep.

In order to detect the crystal growth interface, twelve temperature steps of +0.5°C or +1.0°C were applied during the growth at intervals of 0.5 to 50 h (Fig. 1b). The insert of Fig. 1c shows the first three temperature steps applied at elapsed times of 0 to 5 h. The 1.0°C temperature rise corresponds to a Si concentration change of about 0.2 at. % around the concentration of $Si_{50}Ge_{50}$ from the SiGe phase diagram [40], which produces an artifact striation in the Secondary Electron Microscopy Composition mapping (SEM-COMPO) image. By combining the temperature steps of 0.5°C and 1.0°C and varying the step time intervals, each artifact striation was identified without difficulty. The average growth rate between adjacent striations was calculated from the growth length and the elapsed time.

At the end of crystal growth, the heater power was set to zero, and the heater was moved away from the growing crystal to maintain a sharp

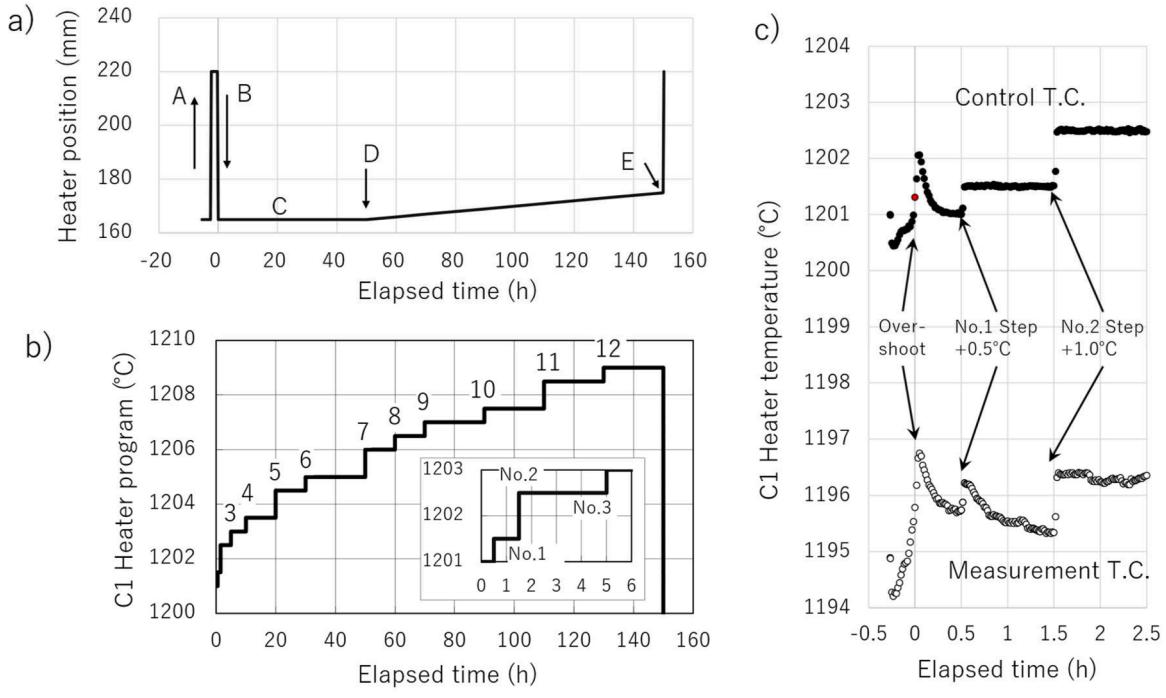

Fig. 1. a) GHF heater moving sequences. A is for preheating, and B is for the preheated heater soaking to form the SiGe melt and initiate SiGe crystal growth. C and D indicate that the heater remains in position. The elapsed time is zero at the end of sequence B. b) Twelve applied heater temperature steps, 0.5 or 1.0, over 150 h. The elapsed time for steps 1 to 3 is shown in the insert. c) Heater temperatures of the primary temperature control and measurement thermocouples through 2.5 h. A rapid heater motion (sequence B) caused a temperature overshoot near zero elapsed time.

growth interface.

3. Results and discussion

3.1. Concentration distribution in the grown SiGe crystal

This section describes the concentration distribution in the grown crystal. The grown crystal was cut parallel to the growth axis. The cut surface was polished with diamond slurry and colloidal silica. A JEOL-8230 electron probe microanalyzer (EPMA) was set to an acceleration voltage of 20 kV and a probe diameter of 2×2 μm^2 to take an SEM image of the cut surface (Fig. 2a). The growth length at the crystal central axis was 18.8 mm during 150 h, a growth rate of 0.125 mm/h. The dissolution distance of the seed Si near the central axis was approximately 0.6 mm, which was shorter than the 2 mm in the ground experiment. The seed/SiGe and SiGe/Zone (remained melt at the end of growth) interfaces are curved parabolically, and their curvatures changed gradually during growth. Since the crystal grows in the direction normal to the S/L interface, the interface must be traced through the growth to accurately calculate the growth rate. Therefore, the growth rate at the central axis (nearly flat interface area) is a good benchmark.

Fig. 2b shows the Si concentration distribution of the crystal's central axis, measured at a 500 μm pitch using EPMA. The average concentration of the grown SiGe crystal of the center axis was $Si_{52}Ge_{48}$. The detailed Si distributions in the initial transient region are described in Section 3.4.

The average temperature gradient dT/dz (K/cm) was calculated using Eq. 1 of TLZ growth model with growth rate V, diffusion constant D (9.5×10^{-5} cm^2/s) [41], S/L concentration difference C_L-C_S (= -33.9 at. %) [40] of Si and 1/m (=1.49×10^{-1} Si at. %/K at $Si_{52}Ge_{48}$) [34], the inverse of the slope of the liquidus line [12]:

$$V = -\frac{D}{m\,(C_L - C_S)}\frac{dT}{dz} \quad (1)$$

The diffusion coefficient D has been applied to SiGe crystal growth experiments in space and on the ground. The calculated dT/dz was 8.3 K/cm.

As shown in Fig. 2b, the Si concentration increased approximately 0.25 at. %/mm from 19.6 mm ($Si_{51.4}Ge_{48.6}$) to 26.1 mm ($Si_{53.0}Ge_{47.0}$), because the growth interface temperature increased with the positive temperature gradient formed by the fixed-position heater. The Si concentration decreased after the growth position of 26 mm in Fig. 2b when the heater was moved from D to E, as shown in Fig. 1. This indicates that the heater's motion was faster than the SiGe crystal growth rate. The speed difference increased the temperature gradient and decreased the temperature on the growth interface [12].

The Si concentration distributions of radial direction at growth lengths of the center-axis of 0.2, 1.0, 3.0, 10, and 18.5 mm, and along the Si-Seed/SiGe interface are displayed in Fig. 2c. To minimize as possible the disturbance of the interface and the inhomogeneity of the Si concentration due to that disturbance, the Si concentration distribution along the Si-Seed/SiGe interface was measured at a distance of about 20 μm from the interface. The Si radial distribution at the interface was convex but became concave as the growth length increased. A uniform concentration distribution was obtained at 3.0 mm. At the growth distances of 10 and 18.5 mm, Si distributions were disturbed in the r>0 region. The Si distribution along the seed/SiGe interface, at the right periphery, was about 2 % lower than in the crystal center area and rapidly increased toward the center axis.

There is a large void in the zone shown in Fig. 2a of the grown SiGe, which was formed during the quenching process at the end of the crystal growth sequence. That is attributed to expansion of volume during solidification at quenching because the feed Si was sufficiently dissolved to grow the SiGe crystal. Therefore, Marangoni convection [42] due to the free melt surface was suppressed during the crystal growth experiment.

Fig. 2d and e are extended SEM photos near the interface between the Si seed, the grown SiGe crystal, and the carbon cell. The Si-seed diameter and the inner diameter of the carbon cell differ by 0.2 mm,

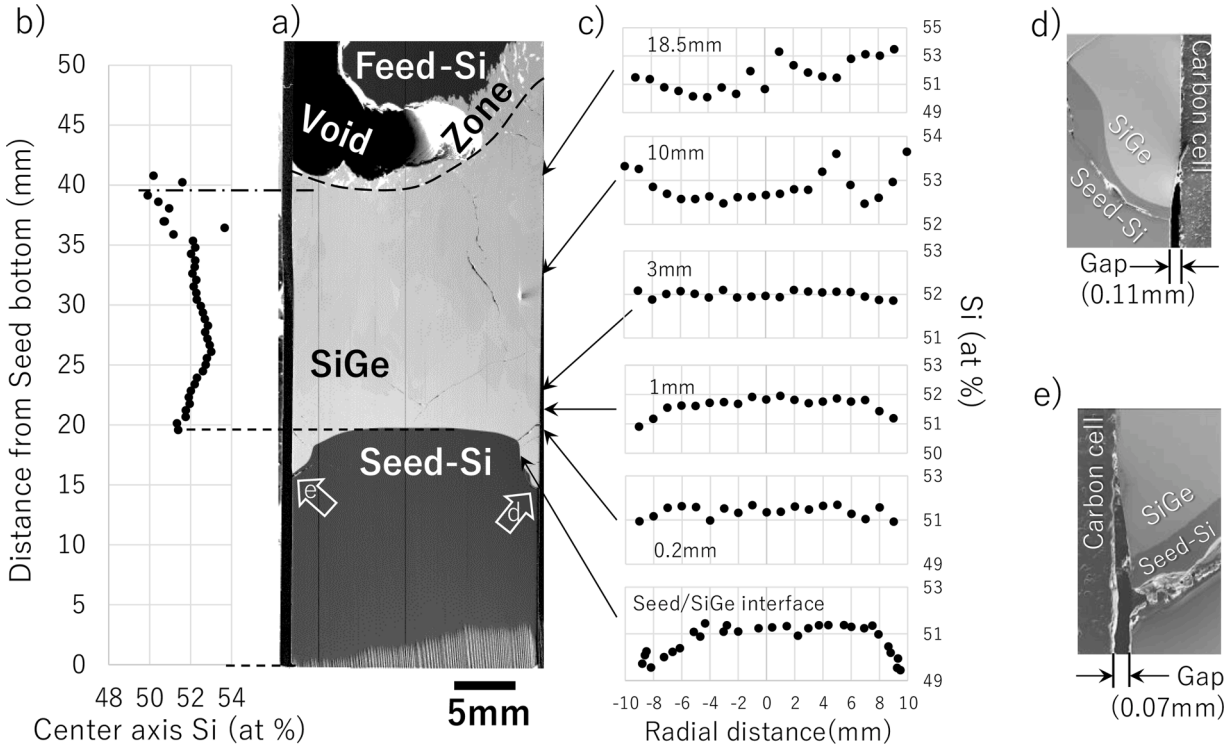

Fig. 2. a) SEM image of the SiGe crystal cross-section grown in the ISS. b) Ge concentration distribution at 500 μm pitch along the center axis of the SiGe crystal shown in Fig. 2a. c) Ge distributions in the radial direction along the seed/SiGe interface, 0.20, 1.0, 3.0, 10, and 18.5 mm growth lengths. d) and e) SEM images around the right and left periphery of the seed/SiGe interface.

and the gap width on the right side (Fig. 2d) is slightly wider than on the left (Fig. 2e). The dissolution depth of the Si seed beside the carbon cell was proportional to the gap width. The seed Si melted more in the peripheral areas than around the center axis area and the Si concentration in the area was lower than the center axis area as shown in Fig. 2c. This indicates that the melted Si at the periphery was supplied to the center during the initial growth stage.

Since the temperature gradient in the peripheral area adjacent to the carbon cell wall was higher than that at the center axis, and solidification proceeded perpendicular to the interface, the gap closed as crystal growth progressed. Please refer to the supplemental information for a discussion of Marangoni convection in the gap. Although these gaps and excessive Si-seed melt-back in the periphery have been observed in previous SiGe space experiments [34,35,37], the correlation with melt supersaturation was not discussed.

3.2. Estimation of the Soret effect in the melt

In long-duration crystal-growth experiments conducted in microgravity, the Soret effect often significantly affects solute transport in the alloy melt [43], so evaluating it is crucial for determining the diffusion constant under a temperature gradient. We have calculated the Soret effect for Si and Ge in a SiGe melt using the model developed by Koyama *et al.* [44]. This model provides the equilibrium concentration distribution at a given temperature gradient and average concentration by the following equation.

$$\frac{\partial G^{\mathrm{Liq}}(c_i, T_i)}{\partial c_i} = \frac{\partial G^{\mathrm{Liq}}(c_j, T_j)}{\partial c_j}, (i, j = 1, 2, \cdots, N)$$

$$\sum_{i=1}^{N} c_i f_i = c_{ave} \tag{2}$$

where G^{Liq} denotes concentration and the temperature-dependent Gibbs energy function of the liquid phase; c_i, T_i, and f_i represent the concentration, temperature, and volume fraction of the i-th region divided into N regions; and c_{ave} is the average concentration of the calculation area. The Gibbs energy data assessed by Bergman *et al.* [45] were employed. The melt concentration of $Si_{17}Ge_{83}$ was in equilibrium with the crystalline $Si_{50}Ge_{50}$ from the Si-Ge phase diagram [40]. In our experiment, the SiGe melt was formed by dissolving pure Ge liquid with a seed and a feed Si [34]. Therefore, we evaluated the Soret effect as the Si concentration gradually increased from zero to $Si_{20}Ge_{80}$. The melt temperature in the experiment reached the crystal growth temperature within several tens of minutes due to the fast heater motion at 600 mm/h described in Section 2 (Fig. 1a). Since the pure Ge melt remained near the S/L interface for only a brief period, the behavior near $Si_{20}Ge_{80}$ is important for assessing the influence of the Soret effect.

Fig. 3 shows the calculated concentration distribution from 927°C to 1127°C (100°C above the $Si_{50}Ge_{50}$ melting point) of the melt with average Ge concentrations of 80, 85, 90, 95, and 99 at. %. Fig. 3 shows that the concentration gradient induced by the Soret effect in the SiGe melt is very small in the given temperature and concentration range. The average concentration change of Si against temperature change ($\Delta c^{\mathrm{Si,soret}}/\Delta T$) is calculated to be -6.0×10^{-3}, -6.0×10^{-4}, 3.2×10^{-3}, 4.5×10^{-3}, and 2.2×10^{-3} Ge at. %/K for the average Ge concentrations of 80, 85, 90, 95, and 99 at. %, respectively. The equilibrium Si distributions in the saturated melt ($\Delta c^{\mathrm{Si,soret}}/\Delta T$) were estimated from the phase diagram [40]: -1.44×10^{-1}, -1.37×10^{-1}, -1.13×10^{-2}, -8.70×10^{-2}, and -6.90×10^{-2} Ge at. %/K, for average Ge concentrations of 80, 85, 90, 95, and 99 at. %, respectively. The -1.44×10^{-1} at. %/K was 24 times the calculated value of -6.0×10^{-3} at. %/K at $Si_{20}Ge_{80}$. Therefore, under current conditions, the influence of the Soret effect on solute transport is negligible.

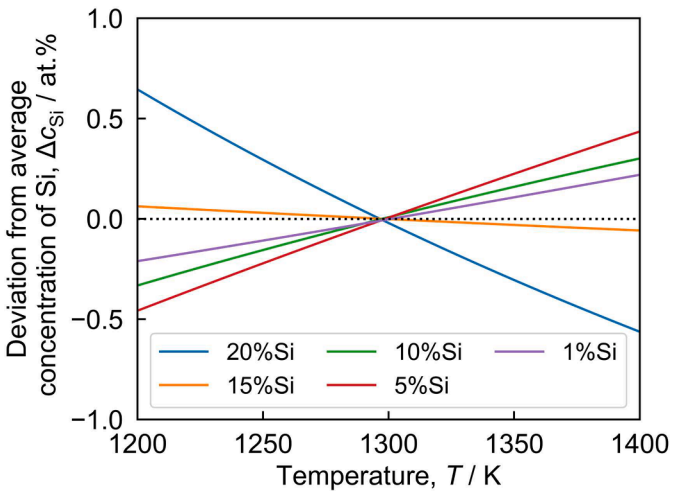

Fig. 3. The calculated equilibrium Si concentration gradient induced by the Soret effect in the SiGe melt with average concentration of $Si_{20}Ge_{80}$, $Si_{15}Ge_{85}$, $Si_{10}Ge_{90}$, Si_5Ge_{90}, and Si_1Ge_{99} (solid lines). The dotted line represents the average concentration of the melt. The variation in Si in SiGe melts due to the Soret effect was small at all calculated concentrations and temperatures.

3.3. Identification of growth interface

3.3.1. Overviews of growth interfaces

The SEM-COMPO image in Fig. 4a is a part of the grown SiGe crystal shown in Fig. 2a, extending from the seed/SiGe interface to a growth length of 12.8 mm. Since the SEM-COMPO contrast is proportional to the backscattered intensity of the irradiated electrons into the crystals, the Si-rich area should appear dark. In fact, the temperature steps by the heater shown in Fig. 1b caused the dark line in the SEM-COMPO image. This method for identifying each striation by the temperature step was the same as that described in the previous report [35]: combining SEM-COMPO images with EPMA concentration measurements.

The dotted yellow lines in Fig. 4a indicate artificial striations 3 to 10 caused by the temperature steps shown in Fig. 1b. Striation 3, except for the center-axis area, had a growth length of about 1 mm and was convex to the melt. Striations 3 around the center axis could not be detected due to crystals remelting from the TGZM effect [46]. This phenomenon occurs when the interface is severely disturbed, leading to the melt being pocketed within the crystal [35]. Combined with the Si concentration distributions in Fig. 2b, c and the convex interface shape, the Si concentration at around striations 3 and 4 (until 3mm of the growth length) tended to decrease from the center axis to the periphery: increase the Si concentration at the center axis with growth and decrease radial concentration distribution toward periphery. Thus, the isothermal contour was flatter than for the growth interface.

Striation 5 at temperature step 5 at 20 h elapsed time in Fig. 1, at about 3 mm growth length, was a flat interface rather than striations 3 and 4, and the radial concentration distribution described in Fig. 2c was homogeneous. This indicated that the striation 5 interface had a homogeneous temperature distribution, and the isothermal contour gradually coincided with the S/L interface. These behaviors differ from those in previous SiGe crystal growth experiments onboard the ISS, which used a 10 mm crystal diameter: the isothermal contour always coincided with the S/L interface [47].

Striations 11 and 12 could not be identified due to the highly disturbed interface caused by polycrystallization. Interestingly, the significant disturbance of the growth interface due to polycrystallization has not been observed in terrestrial SiGe crystal growth. No unexpected nucleation in the melt by constitutional supercooling [37] is observed in Fig. 4a and b.

Fig. 4b shows striations 1 to 3 traced by the dotted yellow lines on the left side of the center axis near the seed/SiGe interface. Striation 1 is

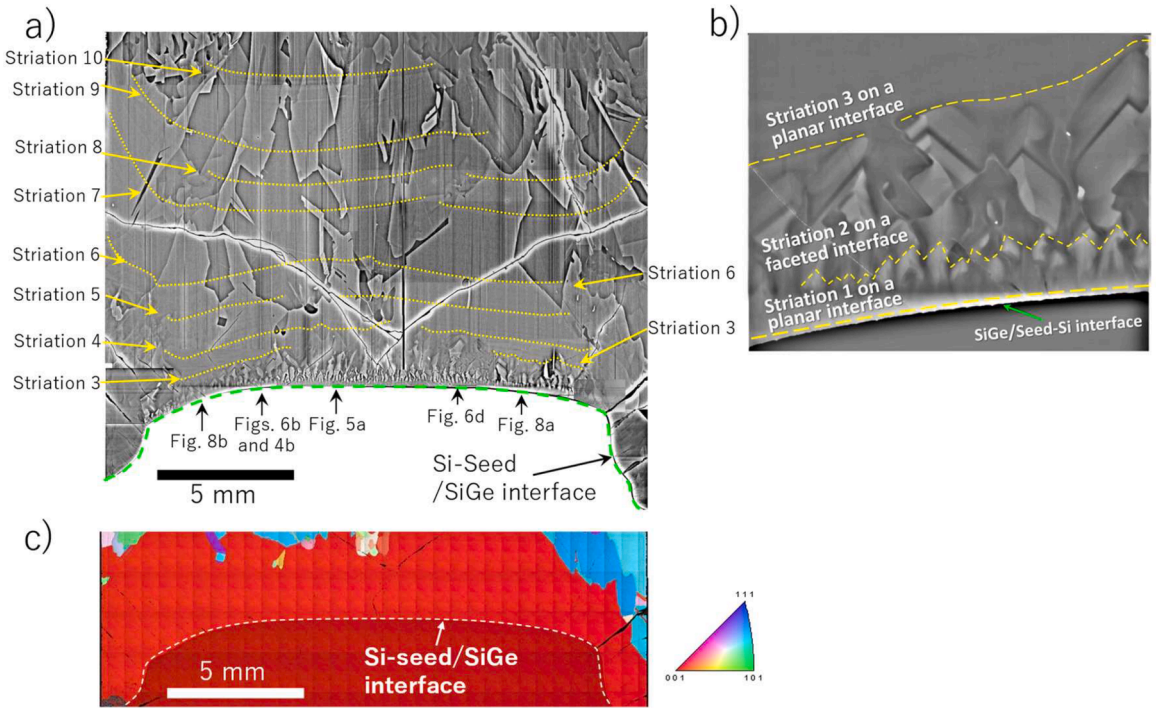

Fig. 4. a) SEM-COMPO image of the SiGe crystal shown in Fig. 2a from the seed/SiGe interface to a growth length of 12.8 mm. The dotted yellow lines trace the artifact striations induced by the temperature steps shown in Fig. 1b. b) Enlarged view around the left of the interface of Fig. 4a. The dotted yellow line indicates striations 1, 2, and 3. c) EBSD image around the seed/SiGe interface. The Si-seed/SiGe interface area in Figs. 4a and b are images of the (100) plane.

parallel to the seed/SiGe interface in this area. Striation 2 is on the facet array, and striation 3 is on the planar interface. To calculate the planar interface growth rates for striations 1 to 2 and 2 to 3, we analyze facet growth in Section 3.3.3. No facets were observed on the right or left periphery near the gap in Fig. 2d and e, but a smooth interface did appear. It was difficult to connect the striations appearing in the peripheral area neighboring the gap to striations 1 to 3 in the center axis area shown in Fig. 4b due to the interface disturbance caused by the TGZM effect [46] described above.

Fig. 4c is the electron backscatter diffraction (EBSD) pattern taken with a 5×5 μm^2 pitch from the seed/SiGe interface to 3.3 mm growth length, and including the part of the seed-Si. The grown SiGe crystal up to striation 4 was a single crystal region.

Although the SiGe melt began to form at time zero, it took about 6 h for the dissolved Si from the Si feed to reach the seed/SiGe interface, as calculated by $L^2=2Dt$ (L: SiGe melt length of 20 mm, $D = 9.5\times10^{-9}$ m^2/s [41]). Thus, the appearance of striation 1 at 0.5 h suggests that the initial SiGe crystal growth occurred by the Si incorporation from the Si dissolved melt from the seed. This growth process differs from the ordinary TLZ growth process, Si dissolved from the feed supplied continuously to the SiGe, but is similar to the unidirectional solidification process. Striation 3 located around the growth length of 1 mm induced by the temperature step 3 (5 h elapsed time) would be grown by nearly saturated melt because it takes 5.3 h for the dissolved Si to reach that interface position.

3.3.2. *Faceting near the seed/SiGe interface*

Since the initial growth regions contain both faceted and planar growth (Fig. 4a), these must be analyzed to calculate the growth rates in Section 3.4.

In the initial growth region, the overshoot and peak in the heater temperature as shown in Fig. 1c significantly affected crystal growth. Temperature step 1, shown in Fig. 1c, is not a step but a broadening sawtooth pulse. Fig. 5a shows the center-axis area in Fig. 4a; striation 1 is a faint dark band about 20 μm wide, indicated by the yellow dotted line just above the seed/SiGe interface. The detailed concentration distribution across striation 1 is presented in Fig. 8d for the growth rate calculation.

Fine facet array patterns were observed after striation 1, around 200 μm from the seed/SiGe interface, as shown in Fig. 5a. Ninety-three facets were distributed over a 15 mm width on the interface, except for the left and right crystal peripheral regions in Fig. 4a. The average spacing of the facet array was 98 μm, with a standard deviation of 24 μm. Additionally, no inclusions were observed in the facet regions in Figs. 4 and 5; therefore, the growth interface instabilities were not caused by impurity condensation in the melt [22,23].

Fig. 5b is an enlarged view of a facet in Fig. 5a. Si concentration distributions over the facet were measured horizontally at a 13 μm pitch over a 60 μm width at six heights, from the lowest position (A) to the highest position (F) shown in Fig. 5c. The Si concentration distributions gradually segregated with growth: the measured Si concentration at 26 and 52 μm were relatively lower than that of the center position (40 μm). These Si segregations remain unchanged after height E. Thus, we defined the facet as having formed at height E from the Fig. 5b and c.

Fig. 5d shows an enlargement of the center of Fig. 5a, where two adjacent facets (from -120 to 0 μm and from 0 to 120 μm) with similar widths of about 100 μm at height G. The solid white arrows trace the center of facets. When the left facet disappeared, the arrow's tilt angle was about 45°. This drift behavior is discussed in Section 3.3.3.

Fig. 5e shows the Si distributions measured with a horizontal 10 μm pitch, corresponding to G to J, as shown by the white dotted lines in Fig. 5d. The measurements were fitted with a smooth curve. Two black arrows around -50 and 75 μm denote the centers of the facets shown by the solid circles on the curves. A constant Si concentration distribution on the right facet (from 0 to 120 μm) during growth from G to J was observed. These indicate that the melt temperature in front of the growing facet were almost constant during growth.

The Si concentrations at the center (solid circles) were about 0.05 at. % higher than those at the adjacent points as shown in curve I. The concentration difference between the inter-facet (radial distance, r=0)

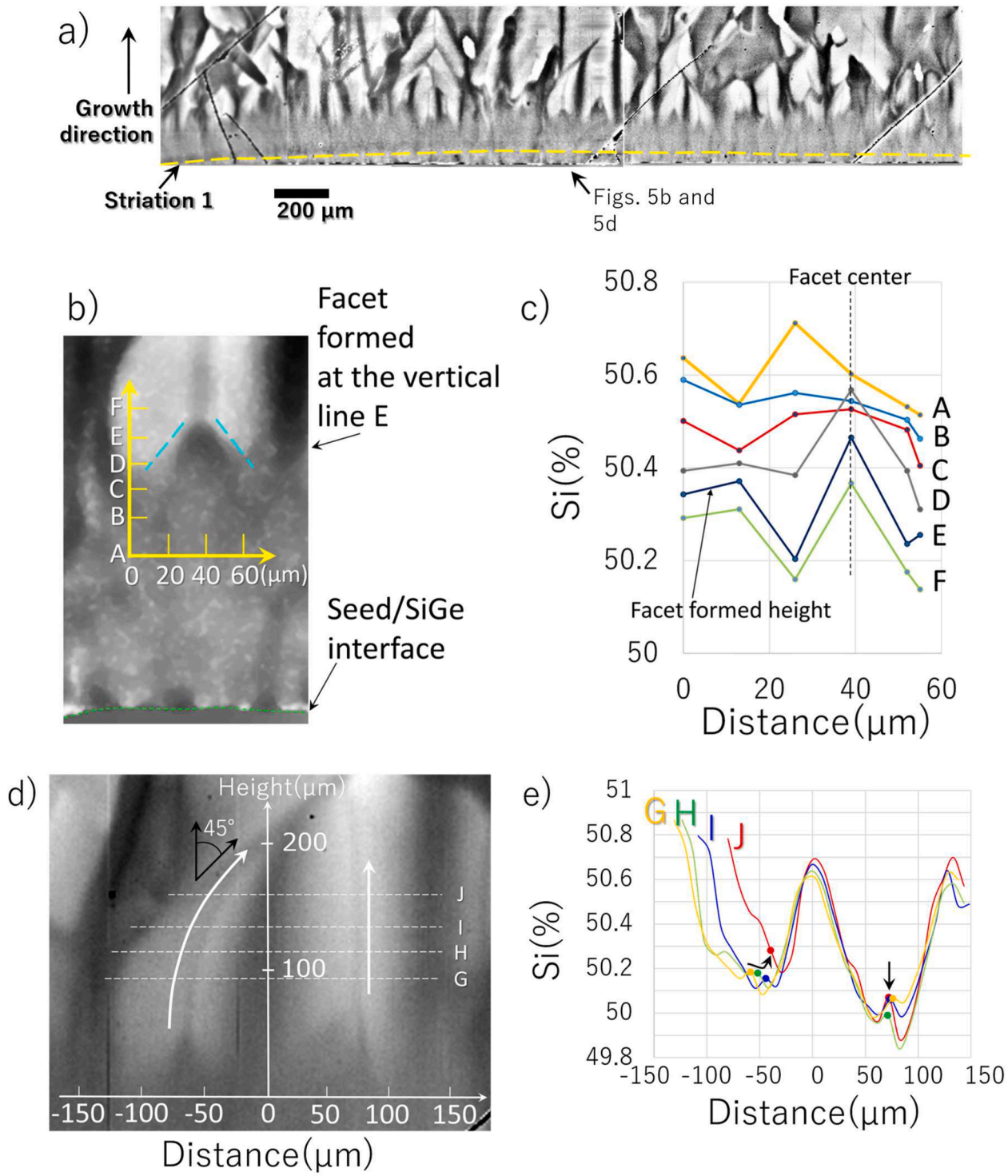

Fig. 5. a) Enlarged view around the center of the seed/SiGe interface in Fig. 4a. b) and c) The SEM-COMPO images around the center of Fig. 5a and the Si concentration distributions of the facet formation region: labels A–F are common to both Figs. 5b and c. d) and e) Enlarged views around the center of Fig. 5a and the Si concentration distributions; labels G–J are common to both Figs. 5b and c.

and the center axis at around 75 μm away is 0.6 at. % for the right facet, while it differed 0.4 at. % between r=0 and the center at -50 μm for the left one.

The left facet (from –120 to 0 μm), having a high Si distribution, might have grown more slowly than the right one with a low Si concentration distribution because the degree of supersaturation is inversely proportional to the Si concentration of the facet. Although the Si concentration distributions in Fig. 5e were not measured along the facet interface, the Si distributions of the left facet seems asymmetric, as indicated by curve J.

Generally, faceted crystals will eventually be bounded by the slowest growing facets: (111) for a SiGe crystal. When there is a difference in the degree of supersaturation between adjacent (111) facets, the lower-supersaturation (lower growth rate) facet occupies more crystal surface area than the higher-supersaturation one. Several models have been proposed for the coarsening of a facet array. Wang *et al.* reported [48]

that facet splitting of the transparent organic solution originates at the high supercooling area, even at the middle of the facet, not necessarily at its peaks or valleys. Tokairin *et al.* [20] reported facet coarsening caused by a difference in the degree of supercooling between adjacent valleys. The facet selection process shown in Fig. 5d may differ from previous models that increase facet spacing due to the disappearance of small facets [49] and the filling of the valleys between them [50]. Namely, the concentration fluctuations between the adjacent facets might cause drift and dissipate through collisions with neighbor ones.

Although Ge condensation at the groove in the valley of SiGe cellular facets during facet growth has been reported [15], we did not detect segregation in our experiments.

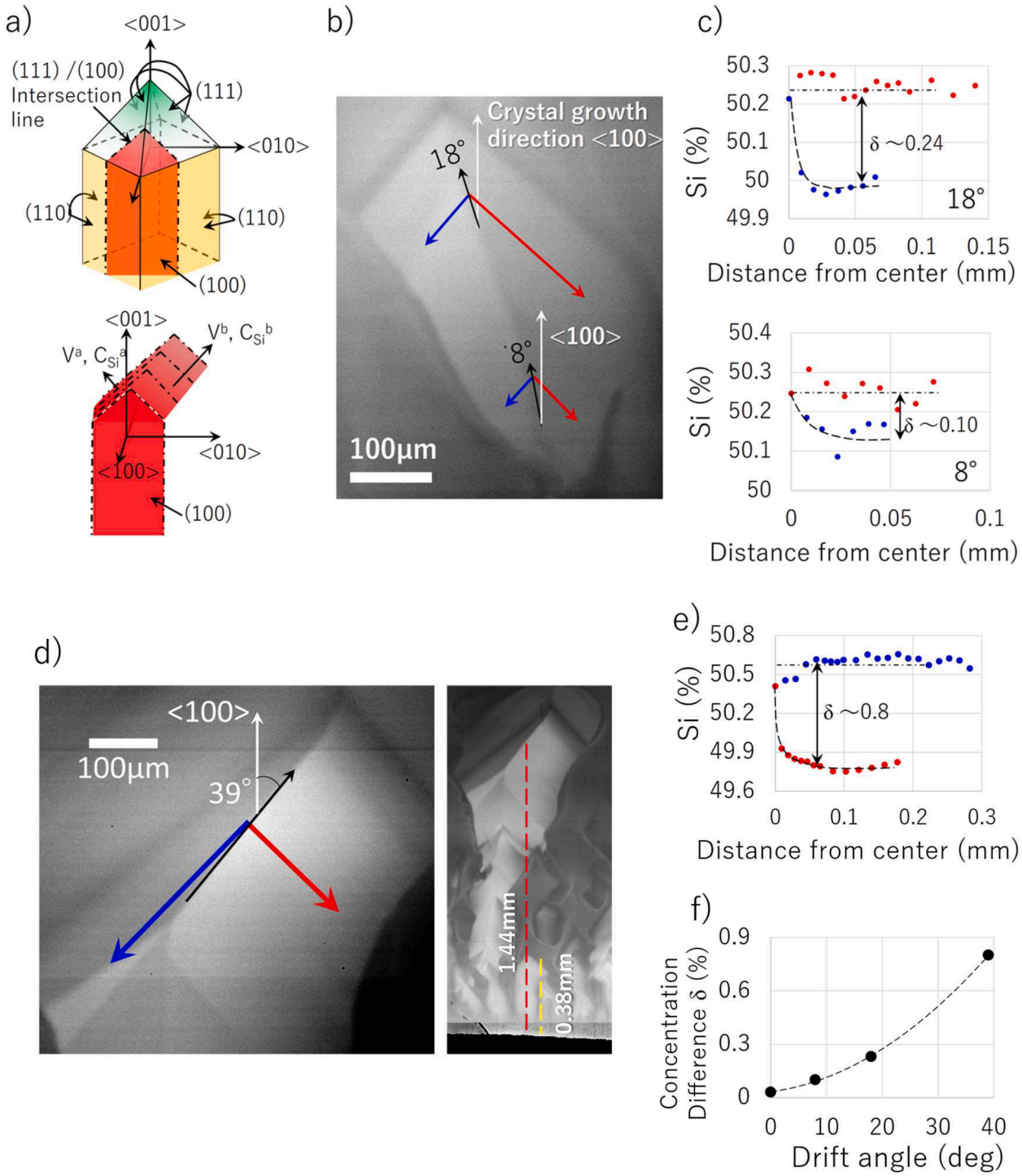

Fig. 6. a) Schematic of a facet. Top row: $<100>_{<110>}$ facet image, Bottom row: (100) cross-sectional image showing the facet drifting to the right during growth. b) Enlarged view of the drift facet in Fig. 4c. The facet boundary (intersection line) observed as a contrast pattern. The 18° and 8° angles are between the <100> growth direction and the facet center-axis trajectory. The red and blue lines are parallel to the terminated lines of the facet. c) Si concentration distributions of the red and blue lines in Fig. 6b. d) Left is magnified SEM-COMPO map of the largest drift angle 39° facet. The right is the reduced figure of the left figure. The facet is located around the right side of the center axis in Fig. 4a. e) The Si concentration distributions on the red and blue lines in Fig. 6d. f) Drift angle dependence of the Si concentration differences δ (Si at. %) between the Si-rich and the Ge-rich facet intersections.

3.3.3. Facet drifting and supersaturations

There are several large facets with a 90° tip angle below striation 3 in Fig. 4b. As shown in Fig. 6a, the geometrical features of the observed facet coincide with the obelisk-like <100>$_{<110>}$ facet in Fig. 7 of Ref. [51]: a 90° tip angle in the (100) and <100> growth directions. In addition, the facet area is the single-crystal region shown in Fig. 4c. The red area enclosed by the dash-dotted line of Fig. 6a; top row is the cross-section image on the (100), and the dash-dotted line is intersection line. The bottom figure shows a schematic of the facet drifting to the right with growing. V_a and V_b are the growth rates of the (111) plane in the <100> direction on the (100) cross section.

Fig. 6b shows the drift of facet growth direction of the second facet from the right in Fig. 4c. That is located around the growth length of 0.60 mm, below striation 3. This facet shape is the cross-section of the facet on (100) as shown at the bottom of Fig. 6a. Thus, if it drifts significantly to the front or behind the crystal cross-section shown in Fig. 4, it is not visible. The leaf-like shape might be due to remelting of the peripheral area caused by increased temperature during the steps.

The 18° and 8° are angles relative to the <100> direction. The angles were deduced by tracing the trajectory of the center axis. The Si concentration distributions were measured from the center axis to the periphery along the intersection lines of the 18° and 8° drifted parts, as shown in Fig. 6c. The blue and red lines are parallel to the top of the facet intersection lines. The angle between lines blue and red is 90 °. The steep decrease in Si concentration near the center (r=0) was on the left blue line in the drift direction. The Si concentrations of the opposite side (red lines) are about 50.25 at. % from the center to the periphery for both angles.

Fig. 6d shows the facet having the largest drift angle, 39°, observed in the center axis area in Fig. 4a. The left figure is enlarged view of the drift facet. The right figure is the reduced map of the left figure. The measured point is located around the growth length of 1.44 mm, below striation 4. Striation 2 was observed the growth length of 0.38 mm below the largest drift facet marked by dotted yellow line. We assumed that the striation 2 position is similar with the length of the largest drift angle facet. Regarding the Si concentration distribution of the 39° drift facet, the large Si concentration difference δ between the red and blue lines (~ 0.8 at. %) was measured and shown in Fig. 6e.

Fig. 6f summarizes the δ values. These values were proportional to the drift angles. Since the Si distributions along both intersection lines (red and blue) were nearly constant, the facet planes would be isothermal from the center to the periphery, except along the center axis. Lower Si concentrations were commonly observed on the drift-side intersection lines compared with those on the opposite side.

Fig. 7a is the schematic diagram of the overlapping of the facet image of Fig. 6b. The distances from line A(B) to line A'(B') corresponds to the (111) facet growth length projected onto the (100) plane as shown in Fig. 6a.

We set three assumptions to calculate the supersaturation in front of the facet shown in Fig. 6b and d, during growth. First, the selected facet was grown parallel to (100). Then, for the simplest model, the melt concentration in front of the facets was homogeneous on both the drifted and non-drifted sides. Since the 1960s, several models have been proposed to discuss the facet growth of metals and Si crystals grown from a melt [52,53]. Third, the simple spiral-growth model (Eq. 2 in Ref. 52) has a growth rate V proportional to $(\Delta T)^2$. In our case, ΔT converted to the supersaturation ΔC using Si-Ge phase diagram [40]:

$$V = k\,(\Delta C)^2 \tag{3}$$

where k is the kinetic constant of the facet surface, and $\Delta C \equiv C_M\text{-}C_F$ (C_F = equilibrium melt Si concentration with measured facet Si concentration, C_M = melt Si concentration) is defined as supersaturation. The growth-rate ratio V^A/V^B, calculated from the distances between A(B) and A'(B') in Fig. 7a, can be correlated with angles α and β (45°) in Fig. 7a. The supersaturation of the i surface $\Delta Ci \equiv C_M\text{-}C_{Fi}$ (i = A and B) can be calculated by:

$$\tan(\beta-\alpha) = \frac{V^A}{V^B} = \left(\frac{\Delta C_A}{\Delta C_B}\right)^2 \tag{4}$$

$$C_M = \left\{C_{FA} - C_{FB}[\tan(\beta-\alpha)]^{1/2}\right\}/\left\{1-[\tan(\beta-\alpha)]^{1/2}\right\} \tag{5}$$

Fig. 7b shows the calculation results. The drift side facets (the Ge-rich side) had higher ΔCi values at each drift angle. And the facet grows faster in the normal direction than on the facet on the opposite, Si-rich side. When both dotted lines for ΔCi were extended to zero, ΔCi was asymptotically close to 0.75 at. %. The melt Si concentrations (C_M) were about 17.3 % (8°), 17.2 % (18°), and 17.4 % (39°): 17.3 at. % ($Si_{17.3}Ge_{82.7}$) melt is equilibrium with $Si_{50.9}Ge_{49.1}$ solid. Although the drifted facets shown in Fig. 6b (8° and 18°) and 6d (39°) are 7 mm apart horizontally and 0.8 mm vertically as shown in Fig. 4a, the melt concentrations ahead of these facets were similar. Under our assumptions, the melt Si concentration may have been uniform from 0.60 to 1.44 mm growth length in the center axis region where many facets appeared.

PFM simulation of SiGe facet growth under the forced Si flow in a SiGe melt exhibited asymmetric facet formation and a weak drift toward the Si-rich luff side under the low temperature gradient (20 K/cm) shown in Fig. 3 of Ref. [17]. In addition, the grown facets seem to have similar concentration distributions on both the luff and lee sides. A drift

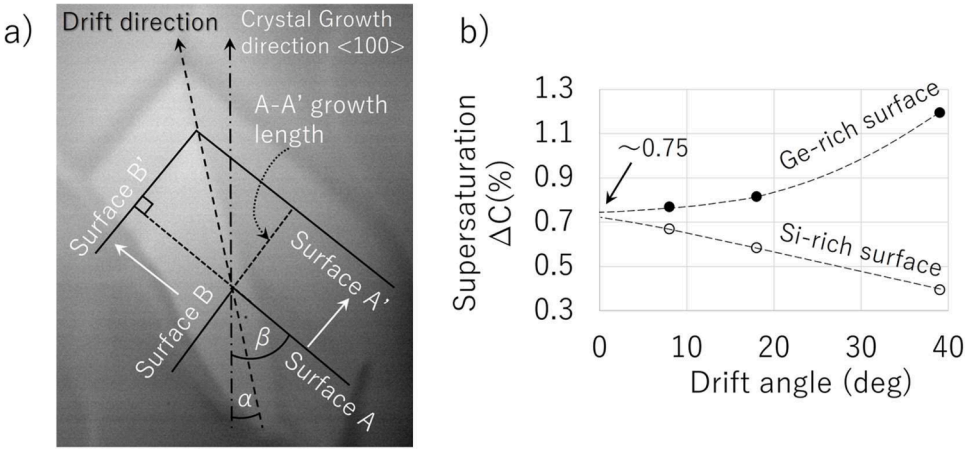

Fig. 7. a) Schematic image of facet surface growth superimposed on Fig. 6b. b) Calculated supersaturation ΔC (%) on the facet surface (intersection lines) of 8°, 18°, and 39° drift facet shown in Figs. 6b and d. Dotted lines are visual guide. Si (Ge)-rich surfaces are the facet intersection lines of red (blue) arrows in Fig. 6b and blue (red) arrow in Fig. 6d left figure.

toward lower Si concentrations was observed in our experiments. The simulation and the present experimental results would indicate facet drift toward the high-supercooling side.

The left facet in Fig. 5d gradually tilted to the right to 45° with growth, and an inclined plane appeared on the left side. In addition, as shown in Fig. 5e, the Si concentration on the left side gradually increased from H to J, whereas that on the right side remained nearly constant.

Since these observations are similar to the feature discussed for Fig. 6 (expansion of the Si-rich facet plane and drift to the opposite side), the facets shown in Fig. 5d were considered to be $<100>_{<110>}$ facets similar to those in Fig. 6b and d.

3.4. Growth rate calculations

The crystal growth rate was calculated using the distances between the striations and the time intervals [35], shown in Fig. 1 and 4a. The crystal growth rates from striations 4 to 8 were calculated by averaging the rates along the central axis and along lines 5 mm from the left and right peripheries, where smooth, flat striations were observed. This method was required to exclude the carbon cell-wall effect and to mitigate the non-axisymmetric feature of striation. Striations 4 to 8 correspond to the temperature step 4 (10 h) to 8 (50 h of elapsed time), as shown in Fig. 1a. The right sides of striations 9 and 10 were unclear; the growth rates were averaged from the rates of the central axis and the left sides. Those calculation methods differ from the rate of striations 4 to 8, but they serve as reference values.

Striation 3 was induced 5 h after the formation of the SiGe melt, by temperature step 3. On striation 3, several bumps are due to facet growth in the initial transition region, as shown in Figs. 4a and b. Striation 3 could not be identified along the center axis due to interface disturbances caused by the TGZM effect [46]. We selected the two flat striation 3 regions to measure the distance between striations 3 and 4 just above Fig. 8a and b. Fig. 8a and b are located 4.6 mm from the right periphery (Fig. 8a) and 3.9 mm from the left (Fig. 8b) per Fig. 4a. The growth lengths of those regions measured at the center axis are lower than 1 mm. Fig. 8b region is closer to the carbon cell wall than the 8a region; the temperature gradient could have increased due to the wall effect, while the striation 3 shape in Fig. 4a and the Si concentrations in Fig. 2b were not significantly different. Thus, the two regions were considered to have similar growth environments. The growth rates from striation 3 to 4 (interval is 5 h in Fig. 1b), just above the regions in Fig. 8a

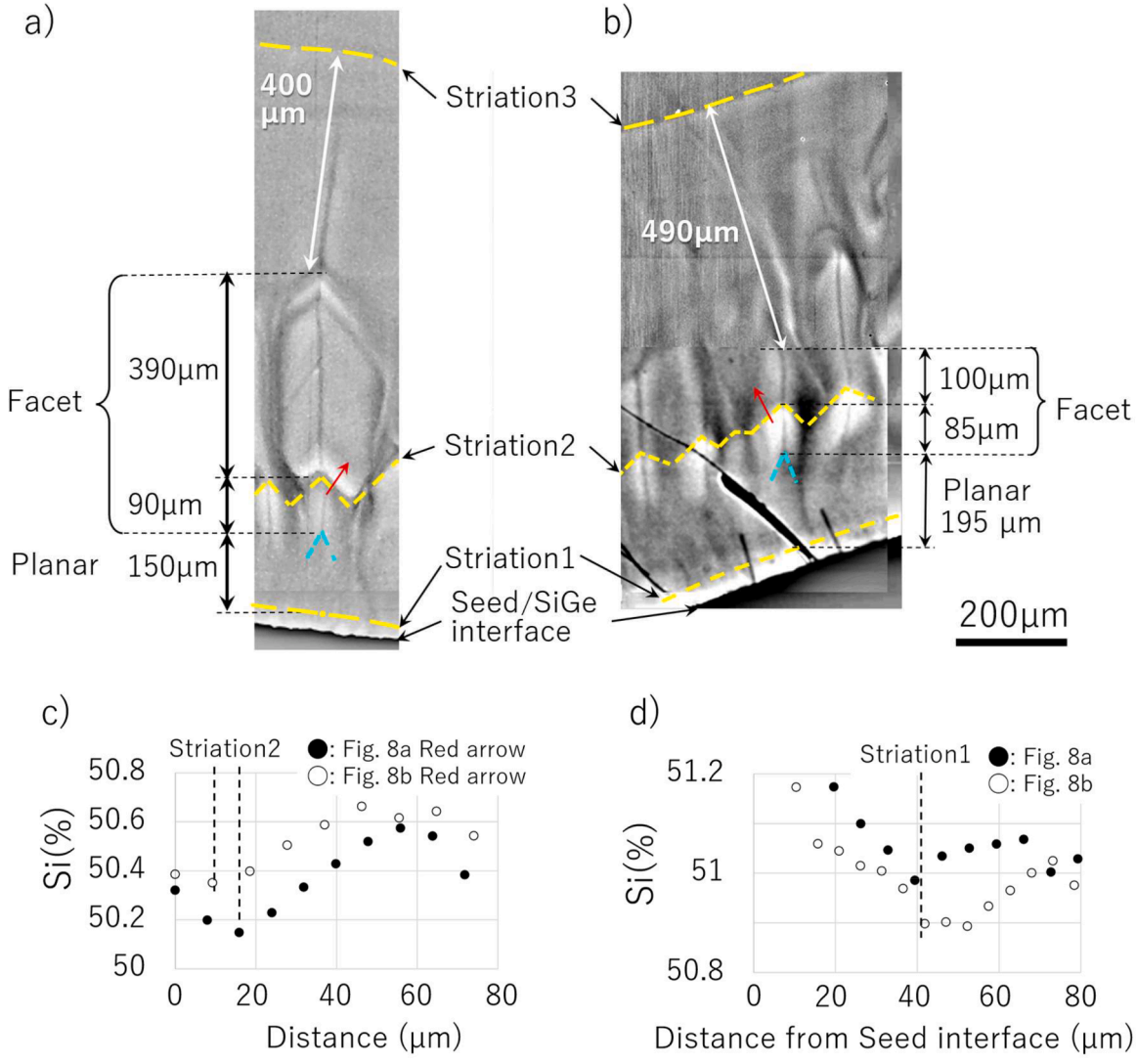

Fig. 8. a) and b) Enlarged views of Fig. 4a, left and right sides. Dotted yellow lines trace striations. Blue chevron-shaped dotted lines indicate the facet formation positions shown in Fig. 5b. The facet-disappearing area is identified where the contrast of the facet image drastically changes. The top of the facet intersection line is defined as the disappearing point. c) Si concentration distribution across striation 2 was measured along the red arrows in Fig. 8a. d) Si concentration distributions across striation 1. Measured lines are directly beneath the top of the facet formation (blue chevron).

and b, were both 0.15 mm/h.

We calculated the facet and planar growth rates individually from striations 2 to 3, shown in Fig. 8a and b, under two assumptions. First, the $<100>_{<110>}$ facet across striation 2 has a similar growth rate from appearance to disappearance. Second, the planar interface growth region occurs before a facet form (Fig. 5a) and after the facet cross-section lines disappear. Additionally, we selected the facet grew vertically without drifting to simplify the growth rate calculation as shown in Fig. 8a and b.

Si distributions of striation 2 shown in Fig. 8c were measured along the red arrows that cross the yellow dotted line in Fig. 8a and b. Striation 2 caused by temperature step 2 (+1.0°C) ideally increase the Si concentration by 0.2 at. % Si for $Si_{50}Ge_{50}$, but the Si concentration rate of increase just after the striation was affected by the concentration fluctuations of the surrounding region. In addition, the two Si distributions in Fig. 8c were similar, suggesting that the two regions in Fig. 8a and b had a similar thermal history.

The Si concentration of solid circle increased from 50.15 at. % (16 μm) at the onset point of striation 2 to 50.57 at. % (56 μm) shown in Fig. 8c. That concentration difference 0.42 at. % indicate the S/L interface temperature increased about 2°C from the Si-Ge phase diagram [40] within the growth length of 40 μm. The excess temperature of 1°C other than the temperature step 2 (+1.0°C) is thought to be due to temperature fluctuations.

Fig. 8d shows the Si distributions across striation 1 in Fig. 8a and b from the seed/SiGe interface. These were measured just below the facet formation points illustrated by the blue dotted lines. The broad sawtooth-shaped temperature step 1 (+0.5 °C) pulse in Fig. 1c was reflected in the increase in 0.1 Si at. % and the gradual increase in the concentration. Striation 1 points in Fig. 8d were identified at 40 μm from the seed/SiGe interface.

Using the growth distances shown in Fig. 8a and b (planar distances 400 and 490 μm and facet distances 390 and 100 μm), the growth rates of the facet and the planar regions between striations 2 and 3 (interval is 3.5 h in Fig. 1) were calculated using simultaneous equations, yielding values of 0.48 mm/h for the facet and 0.15 mm/h for the planar interface. Therefore, the 39° drifted facet in Fig. 6d (around the center axis and about 1.44 mm away from the Seed/SiGe interface) formed 3.7 h elapsed time at the fastest because the striation 2 (1.5 h elapsed) position below the facet is the growth length of 0.38 mm. It is consistent of the difficulty in identifying striation 3 (5 h elapsed time) in the right figure of Fig. 6d. From the calculated melt Si concentration in front of the facet in Section 3.3.3 was 17.4 Si at. %. In Fig. 2c, the average Si concentration of the crystal grown near the growth length of 1.5 mm is $Si_{52}Ge_{48}$ which is in equilibrium with the melt of 18.1 Si at. %. Although concentration fluctuations in the melt must be considered, the melt ahead of the tilted facet was probably close to saturation under our assumptions.

The calculated growth rate of 0.48 mm/h was in the <100> direction for the (111) facet surface. Since the angular difference between <100> and <111> was 35.3°, the normal direction growth rate of the (111) facet was calculated to be 0.51sin (35.3) = 0.28 mm/h.

Combining the calculated growth rate of 0.28 mm/h of (111) facet with the 0.75 at. % supersaturation at the zero angle in Fig. 7b, the kinetic coefficient in Eq. 3 can be calculated to be $k = 1.4\times10^{-6}$ m/s (at. %).

Finally, the growth rate between striations 1 and 2, containing the facet and non-facet regions, in Fig. 8a and b were calculated. The planar growth lengths were 150 and 195 μm in Fig. 8a and b. The facet growth lengths were 90 and 85 μm. The interval between striations 1 and 2 is 1 h in Fig. 1. Here, we used a facet growth rate of 0.48 mm/h, based on the assumptions described above.

Four other areas with features similar to those in Fig. 8a and b, a combination of the facet formation point and striations 1 and 2, could be identified near the 8b region and the center axis region. Therefore, the planar growth rate and standard deviation were derived from six regions. The calculated average planar growth rate and standard deviation were 0.20 mm/h and ±0.026, respectively.

Fig. 9 summarizes the calculated growth rates. The growth rates are expressed as elapsed time, not growth length because of non-axisymmetric striations. Although the averaging procedure for growth rate was changed before and after striation 4 (10 h elapsed time), the tendency for the growth rate in the initial transition region to gradually decrease with elapsed time was confirmed.

3.5. Constitutional supercooling

Using Tiller's criterion [54] of Eq. 6, we assess whether constitutional supercooling occurred in front of the crystal growth interface in the initial transition regions with the high growth rate of 0.20 mm/h as calculated in Section 3.4.

$$\frac{\frac{dT}{dz}}{V} < -\frac{m(C_L - C_S)}{D} \tag{6}$$

To utilize the Eq. 6, measurable values of V, C_S (C_L) and the actual temperature gradient of the melt dT/dz are required. While it is impossible to measure the dT/dz in front of the S/L interface, we can estimate the required temperature gradient during the TLZ growth by using the measured growth rate V and Eq. 1. Eq. 1 is transformed to Eq. 7.

$$\frac{dT}{dz} = -\frac{m(C_L - C_S)}{D}V \tag{7}$$

The dissolved Si from the Si-feed reached near striation 3 (about 1 mm growth length and induced at 5 h elapsed time) after 5.3 h elapsed time as described in Section 3.3.1. After striation 3, the SiGe crystal was grown by the TLZ growth mode as expressed by Eq. 1.

Then, the actual temperature gradient at the start of growth would be estimated by extrapolating the calculated values using the right side of Eq. 7 to the seed/SiGe interface position. To discuss the constitutional supercooling in the initial transition region of Fig. 8a and b, the calculation of the temperature gradient was restricted to the vertical direction of the facets marked by the blue chevron-shaped dotted lines. The calculations were preformed up to striation 6.

Supplemental information Table 1 lists the calculation parameters: C_L-C_S and 1/m calculated by the measured Si concentration, measured growth rate (V) between the adjacent striations, and intermediate growth length (X). This X means the distance from the middle point of

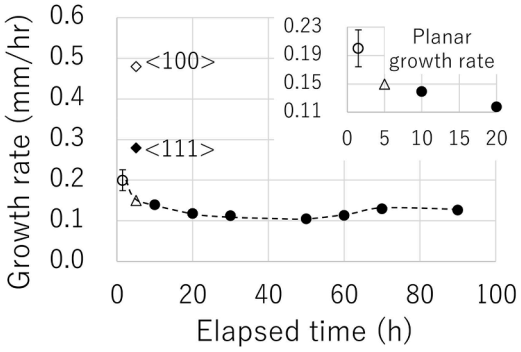

Fig. 9. Elapsed time dependence of the average growth rate of $Si_{52}Ge_{48}$ grown on the ISS. The insert is an enlarged view at the initial elapsed time. Dotted line is a visual guide. Solid circles show the average rate of the planar interface with TLZ growth from striations 3 to 10. The open circle (before faceting) and triangle (disappeared facet) are the rates of plane interfaces. Diamond symbols show the growth rate of the $<100>_{<110>}$ facet. The solid diamond symbol represents the growth rate in the <111> direction of the (111) tip plane, calculated from the <100> growth rate (open diamond) using the geometric arrangement. The average growth rate between adjacent striations is plotted at the longer elapsed time. For example, the growth rate between striations 3 and 4 is plotted as a function of the elapsed time to striation 4 (10 h).

adjacent striations to the seed/SiGe interface measured using Fig. 4a. X=0 mm is the Seed/SiGe interface. The X value between striation 1 and 2 is the intermediated position of the planar regions before appearing the facet as shown in Fig. 8a and b. The growth rates from striation 4 to 5 (0.14 mm/h and 0.10 mm/h in the region of Fig. 8a and b) and from 5 to 6 (0.12 mm/h in both regions) in Table 1 differ by ±0.02 mm/h and +0.01 mm/h from those in Fig. 9.

Fig. 10 summarizes the calculated temperature gradients. The open and solid circles are the temperature gradient of Fig. 8a and b regions. The temperature gradients from 0.7 to 3.8 mm were linearly fitted. The actual temperature gradient at 0 mm, which was about 11 K/cm, was estimated by extrapolating the dotted line to X=0 mm. For this temperature gradient, the required growth rate for the TLZ growth between striation 1 and 2 is calculated at about 0.16 mm/h using Table 1 and Eq. 1. However, the measured growth rate was 0.20 mm/h, which is higher than the required growth rate. When the measured high growth rate is substituted into Eq. 6, it is clear that Tiller's criterion is satisfied between striation 1 and 2.

The planar growth region between striation 2 and 3 around X=0.7 mm after the facets disappeared in Fig. 8a and b, the calculated temperature gradient, 10.0 K/cm, did not deviate significantly from the gradient values thereafter in Fig. 10.

It is speculated that the steep concentration gradient that induced high growth rate was formed as follows. No facet was observed near the gap regions (Fig. 2d and e) as shown in Fig. 4a. But the Si seed was excessively dissolved compared with the central axis region. It suggested that the occurrence of Marangoni convection on the free melt-surface in the gap regions accelerated the transportation of dissolved Si into the melt. But there is no natural convection in the melt. Then, the heater overshoot decreased the equilibrium Si concentration on at the S/L interface. These processes might increase the Si concentration gradient ahead of the S/L interface. While the heater overshoot by several Kelvin might not change the temperature gradient.

On the ground, the high growth rate at the start of the growth is not observed because the dissolved Si in the melt is disturbed by convection and high Si concentration gradient is not formed.

4. Conclusion and summary

We have investigated the growth rate and morphological changes at the growth interface of a bulk $Si_{52}Ge_{48}$ crystal, 20 mm in diameter and 18.8 mm long, grown on the ISS.

Observation of artificial striations due to the temperature step revealed that the SiGe crystal growth rate and the interface shape, including the initial transient region, were affected. The convex S/L interface to the melt at the seed/SiGe interface gradually became concave. The single-crystal length was about 2 mm from the seed-SiGe interface at the center of the crystal.

In the initial transition region, about 1 h after growth started, the crystal growth interface changed from a planar to an obelisk-shaped $<100>_{<110>}$ facet, then returned to planar. During facet growth, the growth direction drifted due to fluctuations in facet concentration: facets on the side with lower Si concentration (higher saturation) grew faster than those on the side with higher Si concentration. The drift angles correlated with the supersaturation on the facet.

The planar growth rate gradually decreased with growth, from 0.20 ±0.026 mm/h nearby the seed/SiGe interface (initial transition region) to 0.11 mm/h after 30 h (about 5 mm growth).

Tiller's criterion was applied to evaluate the constitutional supercooling that resulted in interface instabilities. The observed growth rate of 0.20 mm/h is higher than the expected growth rate of 0.16 mm/h from a saturated melt in front of the S/L interface. Thus, the initial transition region was a constitutional supercooling state. Emergence of the constitutional supercooling is considered to be the result of a combination of non-convection in the melt body, Marangoni convection occurring temporarily at a small free melt-surface in the gap between the seed and the carbon cell wall, and heater overshoot. On the ground, natural convection in the melt probably inhibits the constitutional supercooling under the same heater condition. Further, the calculated Soret effect affecting Si and Ge diffusion in the SiGe melt was very small.

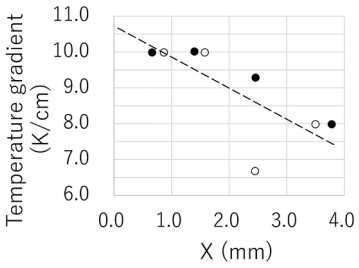

Fig. 10. Calculated intermediate growth length (X) dependences of the average temperature gradient on the vertical direction of Figs. 8a (open circles) and b (solid circles) regions. Dotted linear fitted line is a visual guide.

CRediT authorship contribution statement

Yasutomo Arai: Writing – review & editing, Writing – original draft, Visualization, Validation, Resources, Methodology, Investigation, Formal analysis, Data curation. **Kyoichi Kinoshita:** Writing – review & editing, Writing – original draft, Validation, Supervision, Methodology, Investigation, Conceptualization. **Toshinori Taishi:** Writing – review & editing, Validation, Supervision, Resources, Methodology, Investigation, Data curation, Conceptualization. **Yusuke Matsuoka:** Writing – review & editing, Writing – original draft, Validation, Supervision, Methodology, Investigation, Formal analysis, Data curation, Conceptualization. **Taichi Abe:** Writing – review & editing, Writing – original draft, Validation, Supervision, Methodology, Investigation, Formal analysis, Data curation, Conceptualization. **Takao Tsukada:** Validation, Supervision, Methodology, Investigation, Conceptualization. **Masaki Kubo:** Validation, Supervision, Methodology, Investigation, Conceptualization.

Declaration of competing interest

The authors declare that they have no known competing financial interests or personal relationships that could have appeared to influence the work reported in this paper.

Acknowledgments

The authors would like to extend special thanks to the GHF operators (the GOLEM team members). We greatly appreciate the Materials Fabrication and Analysis Platform at NIMS for measuring and discussing EBSD.

Supplementary materials

Supplementary material associated with this article can be found, in the online version, at doi:10.1016/j.mtla.2026.102709.

References

[1] A.N. Subramanian, C. Richter, A. Gybin, M.P. Kabukcuoglu, E. Hamann, M. Zuber, M. Oezkent, C. Guguschev, U. Juda, T. Schroeder, N.V. Abrosimov, R.R. Sumathi, K.-P. Gradwohl, On the Czochralski growth of Si_XGe_{1-X} crystals as substrates for strained Ge quantum well heterostructures, J. Appl. Phys. 137 (2025) 065704.
[2] M. Nagao, R. Mizoguchi, Y. Shibahara, K. Shikatake, M. Yamada, K. Hamaya, K. Sawano, Complete crack elimination in strained SiGe/Ge(111) heterostructures by pre-patterning of Si(111) substrates, Appl. Phys. Express 18 (2025) 055504.
[3] R. Yokogawa, Y. Arai, I. Yonenaga, M. Tomita, S.Y.Y. Chung, H. Uchiyama, T. Watanabe, A. Ogura, Study on phonon lifetime in bulk silicon–germanium through observation of acoustic phonon spectra broadening by inelastic x-ray scattering, Appl. Phys. Lett. 121 (2022) 082105.

[4] G.L. Bennett, J.L. Lombardo, B.L. Rock, US Radioisotope Thermoelectric Generators in Space, The Nucl. Eng. 25 (1984) 49–58.
[5] Y. Ikoma, T. Yamasaki, T. Shimizu, M. Takaira, M. Kohno, Q. Guo, M.R. McCartney, D.J. Smith, Y. Arai, Z. Horita, Formation of metastable bc8 phase from crystalline $Si_{0.5}Ge_{0.5}$ by high-pressure torsion, Mater. Charact. 169 (2020) 110590.
[6] Y. Arai, Y. Katano, K. Tsubaki, S. Uchida, K. Kinoshita, Silicon-Germanium alloy for infrared GRIN materials, SPIE, Advanced Optics for Imaging Applications: UV through LWIR VI; 117370F (2021).
[7] I. Yonenaga, Growth and Characterization of Silicon–Germanium Alloys, in: G. Kissinger, S. Pizzini (Eds.), Silicon, Germanium, and Their Alloys, Taylor & Francis Group, LLC, 2015.
[8] N.V. Abrosimov, A. Ludge, H. Riemann, V.N. Kurlov, D. Borissova, V. Klemm, H. Halloin, P. von Ballmoos, P. Bastie, B. Hamelin, R.K. Smither, Growth and properties of $Ge_{1-X}Si_X$ mosaic single crystals for γ-ray lens application, J. Cryst. Growth 275 (2005) e495–e500.
[9] D. Labrie, A.E. George, M. Jamieson, S. Obruchkov, J.P. Healey, B.E. Paton, Single crystal growth of $Ge_{1-X}Si_X$ alloys using the traveling solvent method, J. Vac. Sci. Technol. A 22 (2004) 962–965.
[10] N. Armour, S. Dost, Seed Production and Melt Replenishment for the Czochralski Growth of Silicon Germanium, Acta Phys. Polonica A 124 (2013), 198-121.
[11] A.C. Wagner, A. Cröll, H. Hillebrecht, $Si_{1-X}Ge_X$ crystal growth by the floating zone method starting from SPS sintered feed rods – A segregation study, J. Cryst. Growth 448 (2016) 109–116.
[12] K. Kinoshita, S. Yoda, Growth of homogeneous semiconductor mixed crystals by the traveling liquidus-zone method, J. Cryst. Growth 318 (2011) 1026–1029.
[13] S. Pan, M. Zhu, Growth of homogeneous mixed $A_{1-x}B_x$ bulk crystals: analytical prediction, phase-field modeling and experiment comparison, Materialia 5 (2019) 100247.
[14] M. Mokhtari, K. Fujiwara, G. Takakura, K. Maeda, H. Koizumi, J. Nozawa, S. Uda, Instability of crystal/melt interface in Si-rich SiGe, J. Appl. Phys. 124 (2018) 085104.
[15] R. Gotoh, K. Fujiwara, X. Yang, H. Koizumi, J. Nozawa, S. Uda, Formation mechanism of cellular structures during unidirectional growth of binary semiconductor Si-rich SiGe materials, Appl. Phys. Lett. 100 (2012) 021903.
[16] X. Yang, K. Fujiwara, N.V. Abrosimov, R. Gotoh, J. Nozawa, H. Koizumi, A. Kwasniewski, S. Uda, The critical growth velocity for planar-to-faceted interfaces transformation in SiGe crystals, Appl. Phys. Lett. 100 (2012) 141601.
[17] W. Miller, N. Abrosimov, I. Rasin, D. Borissov, Cellular growth of $Ge_{1-X}Si_X$ single crystals, J. Cryst. Growth 310 (2008) 1405–1409.
[18] W. Miller, I. Rasin, D. Stock, Evolution of cellular structures during $Ge_{1-X}Si_X$ single-crystal growth by means of a modified phase-field method, Phys. Rev. E 81 (2010) 051604.
[19] H.K. Lin, H.Y. Chen, C.W. Lan, Adaptive phase field modeling of morphological instability and facet formation during directional solidification of SiGe alloys, J. Cryst. Growth 385 (2014) 44–48.
[20] M. Tokairin, K. Fujiwara, K. Kutsukake, H. Kodama, N. Usami, K. Nakajima, Pattern formation mechanism of a periodically faceted interface during crystallization of Si, J. Cryst. Growth. 312 (2010) 3670–3674.
[21] S.S. Mishra, L.C. Chuang, J. Nozawa, K. Maeda, H. Morito, K. Fujiwara, T. Duffar, Vicinal (111) surfaces at Si solid-liquid interface during unidirectional solidification, J. Cryst. Growth 639 (2024) 127722.
[22] T. Taishi, Y. Ohno, I. Yonenaga, Constitutional supercooling in heavily As-doped Czochralski Si crystal growth, J. Cryst. Growth 393 (2014) 42–44.
[23] I. Yonenaga, T. Taishi, Y. Ohno, Y. Tokumoto, Cellular structures in Czochralski-grown SiGe bulk crystal, J. Cryst. Growth 312 (2010) 1065–1068.
[24] J. Huang, Z. Yin, J. Wu, X. Pan, M. Tang, X. Liu, X. Zhang, InAsSb single crystal with concentrational homogeneity grown in outer space, Natl. Sci. Rev. 12 (2025) nwaf208.
[25] M. Schweizer, M.P. Volz, S.D. Cobb, L. Vujisic, S. Motakef, J. Szoke, F.R. Szofran, Stability of detached-grown germanium single crystals, J. Cryst. Growth 237-239 (2002) 2107–2111.
[26] K. Mazuruk, M.P. Volz, Dynamic stability of detached solidification, J. Cryst. Growth 444 (2016) 1–8.
[27] A.F. Witt, H.C. Gatos, M. Lichtensteiger, M.C. Lavine, C.J. Herman, Crystal Growth and Steady-State Segregation under Zero Gravity: InSb, J. Electrochem. Soc. 122 (1975) 276.
[28] J.J. Derby, Modeling the Growth of Bulk, Single Crystals: Seeing What Is Hidden, Annu. Rev. Chem. Biomol. Eng. 16 (2025) 217–248.
[29] N. Shevchenko, O. Budenkova, G. Chichignoud, S. Eckert, Formation of varying dendritic morphologies in a directionally solidifying Ga-In-Bi alloy, Acta Mater. 288 (2025) 120818.
[30] F. Ngomesse, G. Reinhart, H. Soltani, G. Zimmermann, D.J. Browne, W. Sillekens, H. Nguyen-Thi, In situ investigation of the Columnar-to-Equiaxed Transition during directional solidification of Al–20 wt.%Cu alloys on Earth and in microgravity, Acta Mater. 221 (2021) 117401.
[31] A. Ludwig, J. Mogeritsch, Observations of the occurrence and disappearance of peritectic couple growth performed under microgravity conditions, Scr. Mater. 239 (2024) 115802.
[32] M. Medjkoune, T. Lyons, F.L. Mota, J. Tian, K. Ji, L. Littles, A. Karma, N. Bergeon, Benchmark microgravity experiments and computations for 3D dendritic-array stability in directional solidification, Acta Mater. 292 (2025) 120954.
[33] M. Syvajarvi, R. Yakimova, H.H. Radamson, N.T. Son, Q. Wahab, I.G. Ivanov, E. Janzen, Liquid phase epitaxial growth of SiC, J. Cryst. Growth 197 (1999) 147–154.
[34] K. Kinoshita, Y. Arai, Y. Inatomi, T. Tsukada, H. Miyata, R. Tanaka, J. Yoshikawa, T. Kihara, H. Tomioka, H. Shibayama, Y. Kubota, Y. Warashina, Y. Ishizuka, Y. Harada, S. Wada, T. Ito, N. Nagai, K. Abe, S. Sumioka, M. Takayanagi, S. Yoda, Concentrational uniformity of a $Si_{0.5}Ge_{0.5}$ crystal grown onboard the International Space Station, J. Cryst. Growth 419 (2015) 47–51.
[35] Y. Arai, K. Kinoshita, T. Tsukada, M. Kubo, K. Abe, S. Sumioka, S. Baba, Y. Inatomi, Study of SiGe crystal growth Interface processed in microgravity, Cryst. Growth Des. 18 (2018) 3697–3703.
[36] X. Jin, S. Xu, B. Wang, Y. Okano, J. Yu, Dissolution and growth process of indium gallium antimonide crystal under different gravity levels, Phys. Fluids. 37 (2025) 037115.
[37] K. Kinoshita, Y. Arai, Y. Inatomi, T. Tsukada, H. Miyata, R. Tanaka, Effects of temperature gradient in the growth of $Si_{0.5}Ge_{0.5}$ crystals by the traveling liquidus-zone method on board the International Space Station, J. Cryst. Growth 455 (2016) 49–54.
[38] Y. Inatomi, K. Sakata, M. Arivanandhan, G. Rajesh, V. Nirmal Kumar, T. Koyama, Y. Momose, T. Ozawa, Y. Okano, Y. Hayakawa, Growth of $In_XGa_{1-X}Sb$ alloy semiconductor at the International Space Station (ISS) and comparison with terrestrial experiments, npj Microgravity (2015) 15011.
[39] R. Ghritli, Y. Okano, Y. Inatomi, A. Sekimoto, S. Dost, Estimation of the diffusion coefficient of GaSb in InSb melt using Bayesian optimization and the ISS experimental results, J. Cryst. Growth 573 (2021) 126280.
[40] R.W. Olesinski, G.J. Abbaschian, The Ge-Si (germanium-silicon) system, Bull. Alloy phase Diagr. 5 (1984) 181–183.
[41] S. Adachi, Y. Ogata, N. Koshikawa, S. Matsumoto, K. Kinoshita, I. Yoshizaki, T. Tsuru, H. Miyata, M. Takayanagi, S. Yoda, Homogeneous SiGe crystals grown by using the traveling liquidus-zone method, J. Cryst. Growth 280 (2005) 372–377.
[42] T. Duffar, M.D. Serrano, L. Lerin, J.L. Santaller, Marangoni Convective Effect during Crystal Growth in Space, Cryst. Res. Technol. 34 (1999) 457–465.
[43] E. Sondermann, F. Kargl, A. Meyer, In situ Measurement of Thermodiffusion in Liquid Alloys, Phys. Rev. Lett. 123 (2019) 255902.
[44] T. Koyama, Y. Tsukada, Ludwig–Soret effect formulated from the grain-boundary-phase model, Calphad 73 (2021) 102269.
[45] C. Bergman, R. Chastel, R. Castanet, Thermodynamic investigation on the Si-Ge binary system by calorimetry and Knudsen cell mass spectrometry, J. Phase Equil. 13 (1992) 113–118.
[46] W.G. Pfann, Temperature gradient zone melting, JOM 7 (1955) 9618, 84.
[47] K. Kinoshita, Y. Arai, Y. Inatomi, T. Tsukada, H. Miyata, R. Tanaka, SiGe crystal growth aboard the international space station, J. Cryst. Growth 417 (2015) 31–36.
[48] J. Wang, Y. Inatomi, Three-dimensional Phase Field Modeling of the Faceted Cellular Growth, ISIJ int 50 (2010) 1901–1907.
[49] D.K. Shangguan, J.D. Hunt, Dynamical study of the pattern formation of faceted cellular array growth, J. Cryst. Growth 96 (1989) 856–870.
[50] H.K. Lin, H.Y. Chen, C.W. Lan, Phase field modeling of facet formation during directional solidification of silicon film, J. Cryst. Growth 385 (2014) 134–139.
[51] K. Nagashio, K. Kuribayashi, Growth mechanism of twin-related and twin-free facet Si dendrites, Acta Mater. 53 (2005) 3021–3029.
[52] S.S. Mishra, L.C. Chuang, J. Nozawa, K. Maeda, H. Morito, K. Fujiwara, T. Duffar, Vicinal (111) surfaces at Si solid-liquid interface during unidirectional solidification, Scr. Mater. 247 (2024) 116116.
[53] W. Tiller, The science of crystallization: microscopic interfacial phenomena, Cambridge University Press, 1991, p. 300.
[54] W.A. Tiller, K.A. Jackson, J.W. Rutter, B. Chalmers, The redistribution of solute atoms during the solidification of melts, Acta Metallurgia 1 (1953) 428–437.